Oxygen-incorporated NiMoP nanotube arrays as efficient bifunctional electrocatalysts for urea-assisted energy-saving hydrogen production in alkaline electrolyte

Hao Jiang [a], Mingzi Sun [b], Shuilin Wu [a], Bolong Huang [b], Chun-Sing Lee, Wenjun Zhang [a*]*

[a] Department of Materials Science and Engineering, and Center of Super-Diamond and Advanced Films, City University of Hong Kong, 83 Tat Chee Avenue, Hong Kong, China

[b] Department of Applied Biology and Chemical Technology, The Hong Kong Polytechnic University, Hung Hom, Kowloon, Hong Kong SAR, China

*Corresponding authors.

E-mail address: bhuang@polyu.edu.hk (B. Huang), and apwjzh@cityu.edu.hk (W. Zhang)

Abstract: To couple hydrogen evolution reaction (HER) with urea oxidation reaction (UOR) of a low thermodynamic potential is a promising approach to produce H_2 with reduced energy consumption. However, the development of a low-cost, high-efficiency, and stable bifunctional electrocatalyst toward HER and UOR is still a challenge. In this work, oxygen-incorporated nickel molybdenum phosphide nanotube arrays are synthesized on nickel foam (O-NiMoP/NF) *via* electrodeposition accompanied with *in-situ* template etching. Benefiting from the modulated electronic structure and the nanotube array architecture of O-NiMoP, the self-supporting O-NiMoP/NF electrodes demonstrate highly efficient bifunctional catalytic activity toward HER and UOR in alkaline electrolyte. Particularly, in the HER and UOR (HER||UOR) coupled system for H_2 production, a significantly reduced cell voltage of 1.55 V is obtained at the current density of 50 mA cm^{-2}, which is about 300 mV lower than that of the conventional water electrolysis. Density functional theory calculations reveal that the remarkable HER and UOR activities are originated from the Ni sites with the modulated electronic environment induced by Mo, P and O atoms, which facilitate the water dissociation during HER and balance the adsorption/desorption of the intermediates during UOR. The development of Ni-based phosphides nanotube arrays as a bifunctional electrocatalyst in HER||OER coupled system provides a new approach enabling energy-saving H_2 production.

Keywords: hydrogen evolution reaction, urea oxidation reaction, oxygen-incorporated nickel molybdenum phosphide, nanotube arrays, electrocatalysis

Introduction

As a kind of clean energy source, hydrogen is expected to be an ideal substitute for traditional fossil fuels due to its zero carbon footprints and high gravimetric energy density [1, 2]. Because the current techniques for industrial hydrogen production, *e.g.*, steam reforming and coal gasification involve large consumption of fossil fuels and release of harmful gases including CO_2, electrochemical water splitting has been recognized as a promising alternative to produce hydrogen in a more eco-friendly and sustainable way [2, 3]. Water electrolysis comprises two half reactions, *i.e.*, hydrogen evolution reaction (HER) in cathode and oxygen evolution reaction (OER) in anode; and various electrocatalysts have been recently designed to obtain a high energy conversion efficiency [4-6]. Nevertheless, the large thermodynamic potential (1.23 V) and slow kinetics of anodic OER make hydrogen production through water splitting still a considerably high energy consuming process to be driven at a large voltage (generally $\geqslant$1.8 V) [7, 8]. In this circumstance, to replace OER by other readily anodic reactions with low thermodynamic potentials offers an opportunity to produce hydrogen with reduced energy consumption, and urea oxidation reaction (UOR) is an intriguing substitution owing to its relatively low thermodynamic potential (0.37 V) and potentially cost-free source from urea-rich wastewater [9, 10].

For the anodic UOR process that involves $6e^-$ transfer ($CO(NH_2)_2 + 6OH^- \rightarrow N_2 + 5H_2O + CO_2 + 6e^-$), high-performance electrocatalysts are required to boost the efficiency. Thus far, like those used in HER and OER, noble metal based catalysts (such as Pt, IrO_2 and RuO_2) have been demonstrated to have high catalytic activity for UOR [1, 11]. However, challenges such as high cost and scarcity limit their large-scale applications. Recently, Ni-based catalysts, such as Ni-based alloys, oxides, hydroxides, phosphides, sulfides and their hybrids, have been reported to have impressive electrocatalytic activity toward UOR [12, 13]. Among them, nickel phosphides have shown great application prospects because of their favorable properties such

as high chemical stability, good electrical conductivity and excellent UOR/HER bifunctional activity [14, 15]. Particularly, by incorporating other transition metal atoms to form bimetallic nickel-based phosphides, enhanced UOR electrocatalytic performance is demonstrated [16]. Apart from compositional regulating, structure engineering is another effective strategy to improve the electrocatalytic activity of catalysts. Among the various designed architectures, three-dimensional (3D) nanostructures with enlarged surfaces and rapid charge/mass transfer capabilities, have shown their inherent advantages [12, 17]. Nevertheless, for the 3D nickel-based phosphide nanostructures, the synthesis usually involves high-temperature phosphorization processes and post-etching of templates, which inevitably causes the drawbacks such as the complicated synthesis process and the release of toxic PH_3 gases.

In this work, oxygen-incorporated nickel molybdenum phosphide nanotube arrays were synthesized on nickel foam (O-NiMoP/NF) by electrodeposition accompanied with *in-situ* template etching. The as-prepared O-NiMoP/NF demonstrated excellent bifunctional catalytic activities toward HER and UOR in the alkaline electrolyte. Theoretical calculations based on density functional theory (DFT) were applied to investigate the electronic environments of O-NiMoP, in which the improved activity of Ni sites induced by the neighboring Mo, P and O atoms was revealed to play a predominant role in promoting both HER and UOR. Significantly, when O-NiMoP/NF was employed as the self-supported electrodes for H_2 production in coupled HER||UOR system, only a small cell voltage of 1.55 V was required to deliver a high current density of 50 mA cm^{-2}, which was lower by ~300 mV as compared to that of traditional water electrolysis system coupling HER and OER under the same conditions. The development of Ni-based phosphides nanotube arrays as high-performance bifunctional electrocatalysts for HER and UOR is expected to promote the cost-effective and energy-saving H_2 production technique, and synergistic for the purification of urea-rich wastewater hopefully in the future.

2 Results and discussion

The synthesis processes of oxygen-incorporated nickel molybdenum phosphide nanotube arrays are schematically illustrated in Fig. 1 and Fig. S1. First, ZnO nanorod arrays were grown as templates on nickel foams (ZnO/NF) by the hydrothermal method. The ZnO nanorods were about 1-2 μm in length, and around 100 nm in diameter (Fig. S2). An O-NiMoP film was then deposited on ZnO/NF by electrodeposition in a weak acidic precursor solution (pH~6). After deposition for 10 min, a uniform O-NiMoP thin layer was formed, covering the entire surface of ZnO template (Fig. S3); and as the deposition time was increased to 20 min, the O-NiMoP layer grew thicker and its surface became rougher (Fig. S4). During the deposition of O-NiMoP, the ZnO nanorods were *in-situ* etched in the weak acidic solution, which led to the formation of holes on the tips of some O-NiMoP/ZnO nanorods, as denoted by white circles in Fig. S4b and S4c. The continuous etching of ZnO in this process is supported by the analyses of the corresponding energy dispersive spectroscopy (EDS) and X-ray diffraction (XRD) results in Fig. S5, Table. S1 and Fig. S6. After the deposition of O-NiMoP for 30 min (sample O-NiMoP/NF), the ZnO nanorod template was completely etched away, and O-NiMoP nanotube arrays were constructed on NF, as illustrated in Fig. 1. It was noted that the acidity of the electrodeposition solution had a great impact on the etching of ZnO nanorods, *e.g.*, the O-NiMoP nanotube arrays could not be *in-situ* formed either in neutral (pH=7) or stronger acidic (pH≤5) solutions due to the deficient or excessive etching of ZnO nanorod template during the electrodeposition (Fig. S7). Therefore, controls on the deposition time and acidity of precursor solution are two crucial factors for the successful preparation of O-NiMoP nanotubes by electrodeposition accompanied with *in-situ* template etching.

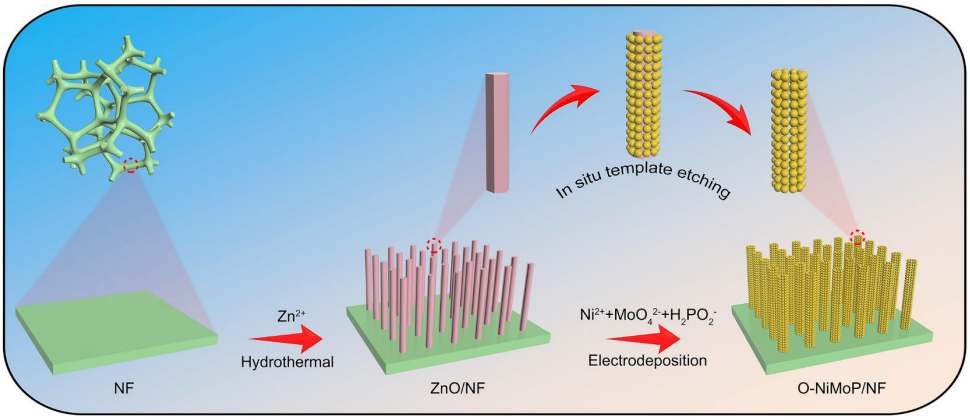

Fig.1 Schematic illustration of the preparation of O-NiMoP/NF.

Fig. 2a to 2c show the scanning electron microscopy (SEM) images of O-NiMoP/NF prepared after deposition for 30 min. Well-defined O-NiMoP nanotubes are observed, and the walls of the nanotubes are composed of interconnected nanoparticles of ~70 nm in diameter. The optical images in Fig. S8 revealed that the color of NF was transformed from sliver-gray to black as the O-NiMoP nanotube array was covered on it. Transmission electron microscopy (TEM) observations further demonstrate the formation of O-NiMoP nanotubes with porous walls, as denoted by the yellow arrows in Fig. 2d. Moreover, O-NiMoP nanotubes are verified to be in the amorphous state, as shown in the high-resolution TEM image (Fig. 2e) and the corresponding selected area electron diffraction (SAED) pattern (Fig. 2f). The scanning TEM (STEM) and corresponding EDS elemental mapping images reveal the uniform spatial distributions of Ni, P, Mo and O elements along the nanotube wall (Fig. 2g to 2k). In addition to the O-NiMoP/NF, oxygen-incorporated nickel molybdenum phosphide nanoparticle film (O-$NiMoP_f$/NF) and oxygen-incorporated nickel phosphide nanotube arrays (O-NiP/NF) were also prepared on nickel foam to comparatively study the effects of 3D nanotube array architecture and alloying on the electrocatalytic activity. The SEM images and EDS spectra of O-$NiMoP_f$/NF and O-NiP/NF are presented in Fig. S9 to S12.

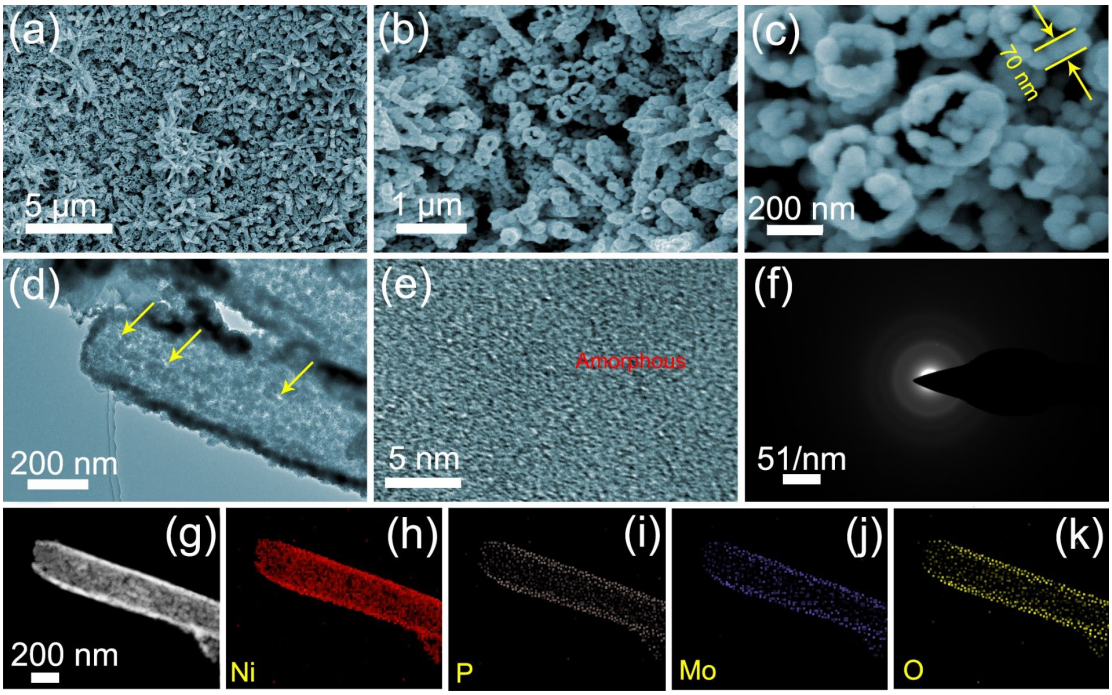

Fig.2 (a-c) SEM images of O-NiMoP/NF with different magnifications. (e) TEM, (f-g) high-resolution TEM images and (g) the SAED pattern of O-NiMoP nanotubes. (i) Dark field STEM and (j-m) the corresponding mapping images of O-NiMoP nanotube.

X-ray diffraction (XRD) patterns in Fig. 3a elucidate only broad diffraction peaks at $2\theta \approx$ 45° for both O-NiMoP and O-NiP nanotubes scraped from NF substrate, which further verifies the amorphous nature of the nanotubes, in accordance with the HRTEM and SEAD results. Based on previous researches, the amorphous alloy surface may have higher electrocatalytic activity, and better corrosion resistance and mechanical strength as compared to their crystalline counterparts[18, 19]. The surface chemical compositions of O-NiMoP and O-NiP nanotubes were acquired through the X-ray photoelectron spectroscopy (XPS) analysis. The XPS survey spectra indicate the presence of Ni, Mo, P and O elements in O-NiMoP nanotubes, while only Ni, P and O signals are observed on O-NiP nanotubes (Fig. S13). The incorporation of O atoms in the as-prepared samples could be originated from the surface oxidation during

the preparation process or post-growth exposure to air. In the high-resolution Ni 2p spectra (Fig. 3b), two peaks at 852.9 and 870.2 eV are ascribed to the nickel in Ni-P, and the peaks at 856.1 and 873.8 eV correspond to nickel in the oxide state [10, 20, 21]. In addition, the remaining two peaks locate at 861.2 eV and 880.3 eV are assigned to shakeup satellites [22]. For the Mo 3d spectrum of O-NiMoP nanotubes (Fig. 3c), the peaks centered at 228.2 and 231.4 eV are originated from Mo-P bonding, and the peaks at 229.5 and 232.7 eV are attributed to the Mo-O components [20]. As regards the P 2p spectra (Fig. 3d), the peaks at 129.7 and 130.6 eV correspond to Ni/Mo-P in metal phosphides, and the broad peak at approximately 133.2 eV is due to the formation of P-O species on the samples [22, 23].

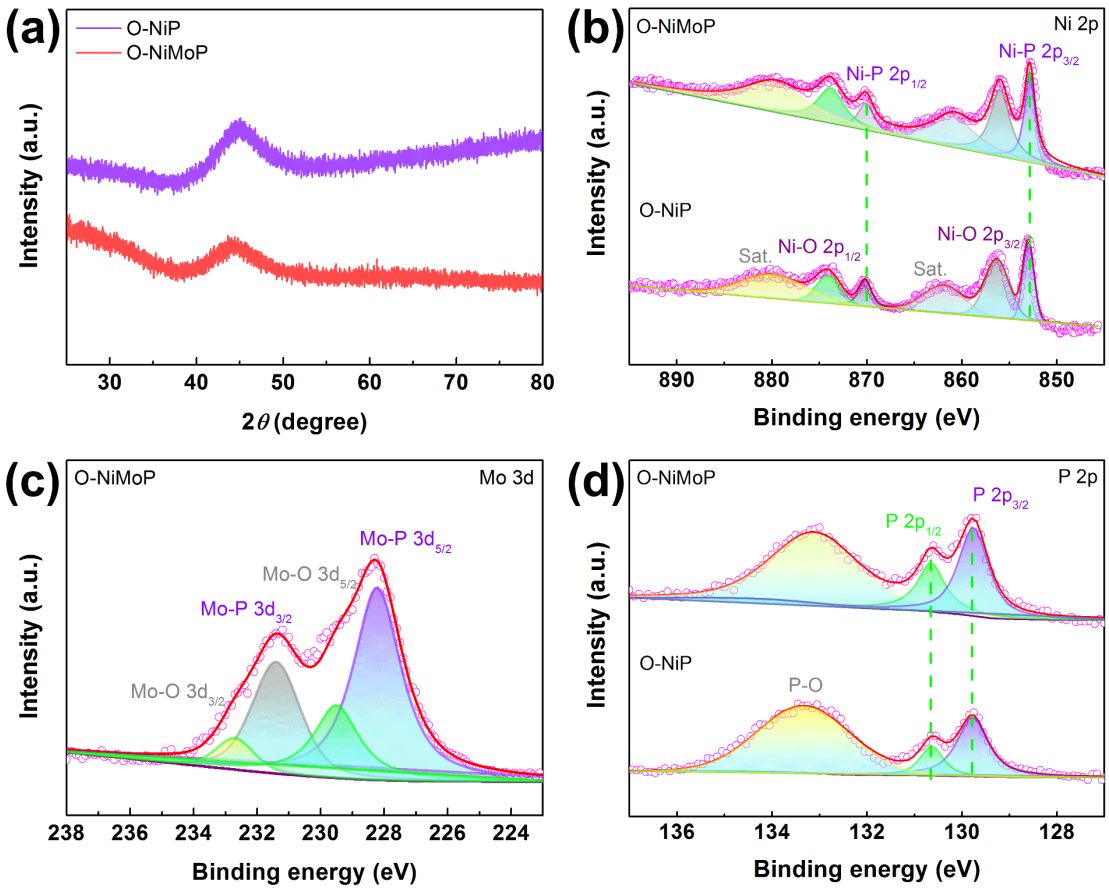

Figure 3. (a) XRD patterns of O-NiP and O-NiMoP nanotubes scraped from NF substrates. High resolution XPS spectra of (b) Ni 2p, (c) Mo 3d and (d) P 2p collected from O-NiP and O-

NiMoP nanotubes.

Catalytic activity towards UOR.

The UOR catalytic activity of O-NiMoP/NF was primarily evaluated in 1.0 M KOH with 0.5 M urea. As presented in Fig. 4a, a small UOR onset potential of 1.30 V (vs. RHE) is obtained for O-NiMoP/NF, beyond which the current increases sharply, and a current density of 100 mA cm^{-2} for UOR is achieved at only 1.41 V (vs. RHE). In comparison with the OER performed in 1.0 M KOH, the potential is sharply reduced by 340 mV to deliver the same current density of 100 mA cm^{-2}. Meanwhile, at the applied potential of 1.41 V, O-NiMoP/NF exhibits an increased UOR current density of about 1.3-fold to 13.5-fold larger than those of O-$NiMoP_f$/NF, O-NiP/NF, RuO_2/NF and NF (Fig. 4b). It demonstrates that the increased active surface exposed by the 3D nanotube array architectures and the remodeled electronic structure induced by introducing Mo atoms into Ni-P skeletons significantly enhance the UOR activity of O-NiMoP/NF. The UOR activity of O-NiMoP/NF is also comparable to those of prominent non-noble metal catalysts reported to date, *e.g.*, NiClO-D [24], Ni_2P/MoO_2/NF [10], NiMoO/NF [9], Pt/C catalyst [25], and as well some more reports as summarized in Table S2. The influences of urea concentrations and scan rates on the UOR activity of O-NiMoP/NF are also investigated. Apparently, the optimal UOR activity of O-NiMoP/NF was achieved as the urea concentration was higher than 0.5 M (Fig. S14). The little variation of current density as the scan rate increases from 5 mV s^{-1} to 100 mV s^{-1} illustrates an outstanding charge transfer capability of O-NiMoP/NF in UOR process (Fig. S15).

To explore the reaction kinetics of these catalysts, Fig. 4c displays the corresponding Tafel slopes derive from their UOR polarization curves. O-NiMoP/NF possesses a Tafel slope of 34 mV dec^{-1}, which is smaller than those of O-$NiMoP_f$/NF (35 mV dec^{-1}), NiP/NF (40 mV dec^{-1}),

RuO_2/NF (56 mV dec^{-1}) and NF (67 mV dec^{-1}); and the results suggest its rapid electron transfer rate and superior UOR catalytic kinetics [25]. In addition, electrochemical impedance spectroscopy (EIS) was also carried out to study the UOR kinetics of these catalysts, as shown in Fig. 4d and Fig. S16. The smallest value of charge transfer resistance (R_{ct}) obtained from O-NiMoP/NF (1.6 Ω) is in accordance with its smallest Tafel slope and further verifies its outstanding UOR charge transfer kinetics.

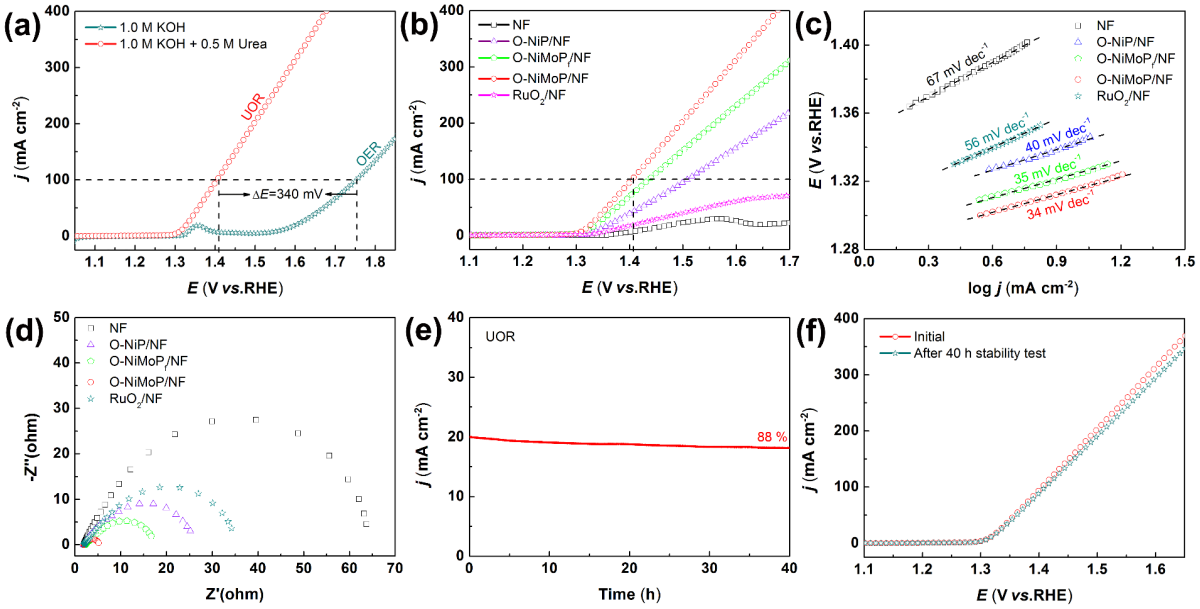

Fig.4 (a) Polarization curves for the OER and UOR of O-NiMoP/NF in 1.0 M KOH + 0.5 M urea with a scan rate of 5 mV s^{-1}. (b) UOR polarization curves, (c) the corresponding Tafel slopes and (d) Nyquist plots of NF, O-NiP/NF, O-NiMoP$_f$/NF, O-NiMoP/NF and RuO_2/NF in 1.0 M KOH+0.5 M urea. (e) The chronoamperometry response of O-NiMoP/NF at 1.33 V (vs. RHE) for UOR. (f) Polarization curves of O-NiMoP/NF before and after UOR stability tests with a scan rate of 5 mV s^{-1}.

The long-term stability of a catalyst is another important property to be considered for its practical application. Fig. 4e presents the chronoamperometric response of O-NiMoP/NF at

1.33 V in 1.0 M KOH with 0.5 M urea. A retention rate of about 88 % is achieved for the current density after the O-NiMoP/NF is continuously operated for 40 h, demonstrating its favorable stability toward UOR in the alkaline medium. In addition, the linear sweep voltammetry (LSV) measurements of O-NiMoP/NF were performed in the fresh electrolyte before and after the 40 h's stability test. As shown in Fig. 4f, only a little variation of the LSV curves is revealed. Together with the chronoamperometry test, the above results clearly demonstrate that O-NiMoP/NF owns remarkable electrocatalytic stability toward UOR in an alkaline environment.

Catalytic activity towards HER.

The HER catalytic activity of O-NiMoP/NF was also investigated in the Ar-saturated 1.0 M KOH electrolyte. The polarization curves in Fig. 5a show that O-NiMoP/NF holds an overpotential of 54 mV at the current density of 10 mA cm^{-2}, which is drastically lower than those of O-$NiMoP_f$/NF (97 mV), O-NiP/NF (138 mV) and NF (240 mV). Remarkably, the HER activity of O-NiMoP/NF is comparable to that of Pt/C/NF electrode, and for the current density higher 100 mA cm^{-2}, even a smaller overpotential of O-NiMoP/NF is required to deliver the same current density, demonstrating the prominent HER catalytic activity of O-NiMoP/NF in a wide potential range (Fig. 5b). In comparison with some representative transition metal-based catalysts reported thus far, the performance of O-NiMoP/NF is among the best of them, as summarized in Table S3. Furthermore, the concomitant urea (0.5 M) in the electrolyte is demonstrated to have a negligible impact on the HER activity of O-NiMoP/NF (Fig. S17), suggesting the capability of O-NiMoP/NF to be used as an electrode for promoting H_2 production in the HER||UOR coupled system.

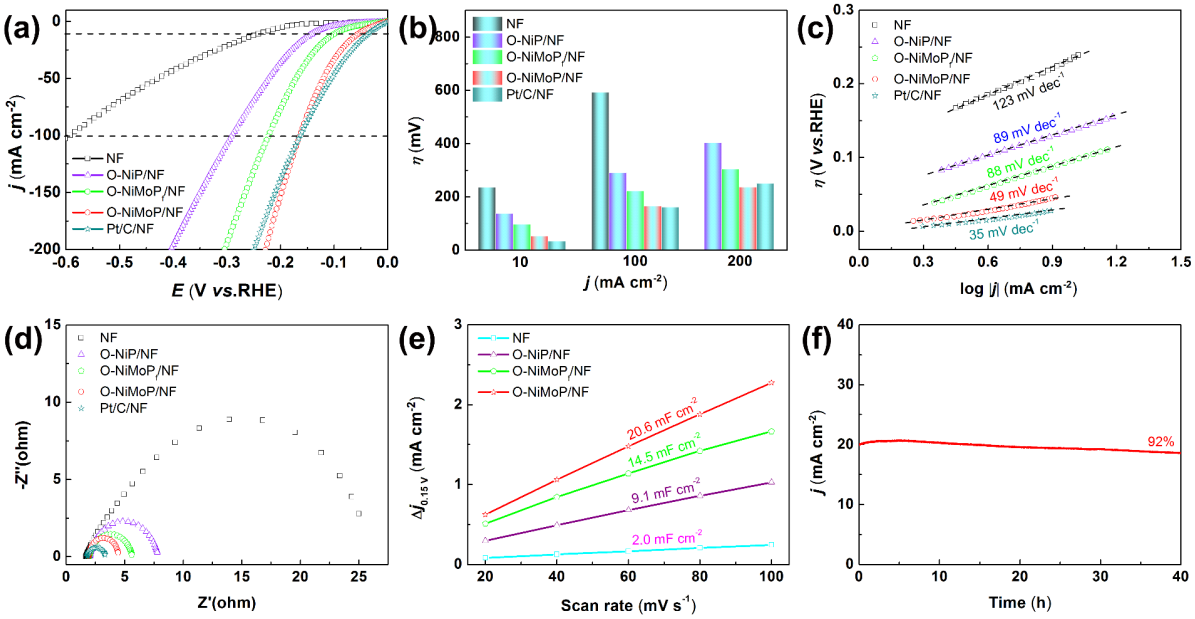

Fig. 5 (a) HER polarization curves of NF, O-NiP/NF, O-NiMoP$_f$/NF, O-NiMoP/NF and Pt/C/NF in 1.0 M KOH with a scan rate of 5 mV s^{-1}. (b) Comparison of overpotentials (η) of different catalysts at selected current densities. (c) The corresponding Tafel slopes, (d) Nyquist plots and (e) C_{dl} value of the above catalysts. (f) The chronoamperometry response of O-NiMoP/NF at η=80 mV for HER.

To analyze the electrocatalytic kinetics of the catalysts for HER, the Tafel slopes of the samples are presented in Fig. 5c. It is revealed that the Tafel slope of O-NiMoP/NF only slightly overtops that of Pt/C/NF, but is much lower than those of other catalysts, suggesting its favorable HER kinetics similar to Pt/C/NF and follows a Volmer-Heyrovsky mechanism in alkaline media [26, 27]. The excellent kinetic property of O-NiMoP/NF is also verified by its low R_{ct} (Fig. 5d and Fig. S18), which guarantees the effective combination of electron and adsorbed hydrogen (H*) during the electrocatalytic HER process [28]. Additionally, the double-layer capacitance (C_{dl}), which is proportional to the electrochemically active surface area (ECSA) of the samples, was measured by cyclic voltammetry to evaluate their intrinsic catalytic activities (Fig. S19). The C_{dl} value of O-NiMoP/NF (20.6 mF cm^{-2}) is much higher

than those of O-NiMoP$_f$/NF (14.5 mF cm^{-2}) and O-NiP/NF (9.1 mF cm^{-2}), and is nearly 10 times of that on NF (2.0 mF cm^{-2}), demonstrating that O-NiMoP/NF has a much higher density of active sites for HER (Fig. 5e). Finally, the electrochemical stability of O-NiMoP/NF electrode toward HER is verified by its high current retention (92 %) after successive operation for 40 h at an overpotential of 80 mV (Fig. 5f). The 3D nanotube array structure of O-NiMoP/NF is favorable for preventing its aggregation and Ostwald ripening, and thus enabling the long-time stability of O-NiMoP/NF in the electrocatalytic process.

Catalytic activity towards overall electrolysis

Considering the superior bifunctional electrocatalytic performance of O-NiMoP/NF electrode toward both HER and UOR, an energy-saving H_2 production system was constructed by coupling HER and UOR using O-NiMoP/NF as self-supporting electrodes, as shown schematically in Fig. 6a. For comparison, the conventional water electrolysis system coupled HER and OER was also established using the same electrodes. As revealed by the polarization curves in Fig. 6b, the HER||UOR system equipped with O-NiMoP/NF electrodes only require a cell voltage of 1.36 V to achieve a current density of 10 mA cm^{-2}, which is much smaller than that of the conventional HER||OER system (1.58 V). Meanwhile, at the cell voltage of 1.55 V (corresponding to the current density of 50 mA cm^{-2}), the HER‖UOR system presents almost a 6.6-fold improvement of current density in comparison with that in water electrolysis, suggesting that substituting OER with more readily UOR is an effective strategy for energy-saving H_2 production (Fig. 6c). Furthermore, the overall electrocatalytic property of O-NiMoP/NF is even superior to that of noble metal-based catalysts in the same HER||UOR coupling system, *i.e.*, a cell voltage of 1.36 V *vs.* 1.46 V of Pt/C/NF‖RuO_2/NF at the current density of 10 mA cm^{-2}. Significantly, the effectiveness in reducing the cell voltage becomes more evident with the increase of current density (Fig. S20). For example, at a current density of 50 mA cm^{-2}, the cell voltage of HER||UOR coupling system using O-NiMoP/NF electrodes

sharply decreased by 260 mV as compared with that of using Pt/C/NF||RuO_2/NF electrodes (Fig. 6d).

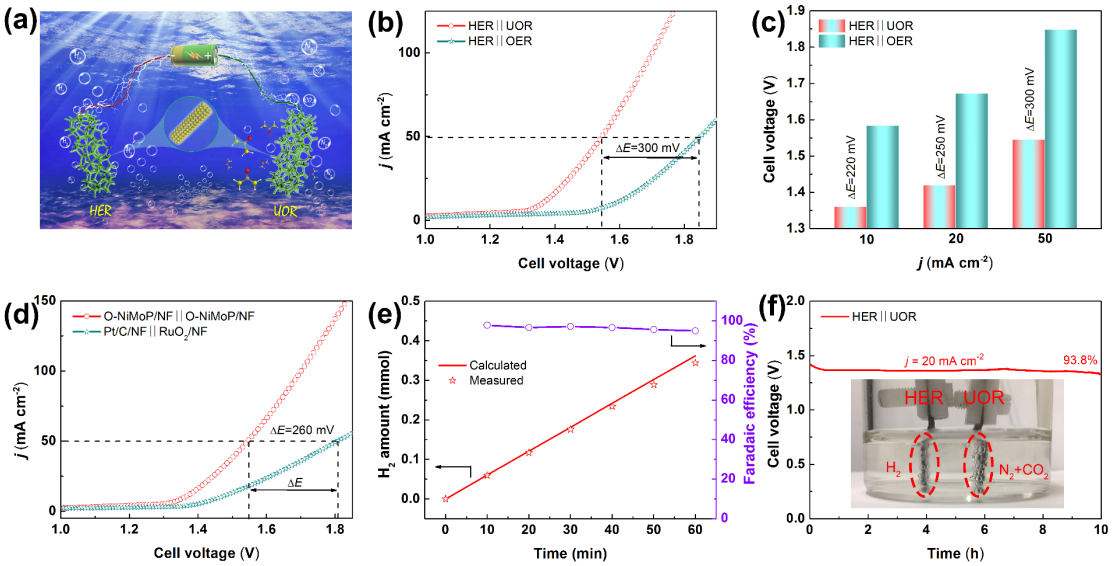

Fig. 6 (a) Schematic illustration of HER||UOR coupled system using O-NiMoP/NF as bifunctional electrodes. (b) Polarization curves of O-NiMoP/NF electrodes in HER||UOR and HER||OER coupled systems. (c) Comparison of cell voltage for HER||UOR and HER||OER systems at different current densities. (d) Polarization curves of O-NiMoP/NF couple and Pt/C/NF||RuO_2/NF electrodes in HER||UOR system. (e) Faradaic efficiency of H_2 production in HER||UOR system upon operation time. (f) Cell stability test of O-NiMoP/NF electrodes in HER||UOR system at a current density of 20 mA cm^{-2}. The inset shows the optical image of the test system, and bubbles of H_2 and N_2+CO_2 can be observed on the O-NiMoP/NF cathode and anode, respectively. The electrolytes for HER||OER system and HER||UOR system are 1.0 M KOH and 1.0 M KOH with 0.5 M urea, respectively.

Video. S1 shows the H_2 generation process in the HER||UOR system as the cell voltage is increased from 1.0 to 1.7 V. It can be seen that the N_2 and CO_2 bubbles are firstly produced *via*

UOR from anode at a low cell voltage, and then continuous H_2 bubbles are vigorously generated and rapidly escaped from the cathode. It demonstrates that the 3D O-NiMoP nanotube arrays not only benefit the infiltration of electrolyte and reactants but also provide efficient diffusion pathways for the rapid release of gaseous products. By quantifying the H_2 produced (Fig. S21), the Faradaic efficiency for HER is calculated to be 96.8 % (Fig. 6e), illustrating a great capability of O-NiMoP/NF for H_2 production in the HER||UOR system. Furthermore, no obvious activity degradation was observed after continuous H_2 generation at a high current density of 20 mA cm^{-2} for 10 h (Fig. 6f), highlighting the outstanding stability of O-NiMoP/NF electrodes. The integrity of the 3D nanotube architecture of O-NiMoP is well preserved after the long-term H_2 production operation (Fig. S22). In comparison with the non-noble metal-based catalysts reported thus far (Table S4), the O-NiMoP/NF electrodes show a preeminent overall performance, suggesting that the O-NiMoP/NF could be worked as promising self-supporting electrodes for the energy-saving H_2 production in HER||UOR system.

Catalytic mechanisms revealed by DFT computations.

To understand the excellent electrocatalytic activity of O-NiMoP/NF for both UOR and HER, density functional theory (DFT) calculations were carried out to reveal the underlying catalytic mechanisms. According to the experimental characterizations, the atomic structure model of amorphous O-NiMoP is constructed, where Ni, Mo, and P atoms are more abundant in the near-surface regions while O atoms mostly locate on the surface regions (Fig. 7a). As demonstrated in the 3D contour plot of the anti-bonding and bonding orbitals near Fermi level (E_F), both O-NiMoP and O-NiP show strongly disturbed electronic distributions (Fig. 7b and 7c). In comparison with O-NiP, O-NiMoP has more bonding orbitals near the surface, indicating a higher preference for electron transfer. Notably, surface O sites in O-NiP have significantly contributed to the bonding orbitals while Ni sites are more active in O-NiMoP. The different electronic distributions of O-NiMoP are attributed to the additional Mo atoms in

the near-surface regions. To obtain more information on the electronic structures of O-NiMoP, the projected partial density of states (PDOSs) of each element is demonstrated in Fig. 7d. In particular, Ni-3d orbital displays a close peak to E_F at E_V-0.88 eV, which acts as the active site to support fast electron transfer with low energy barriers. Meanwhile, Mo-4d orbital exhibits a broad range, which not only protects the robust valence of Ni sites but also facilitates the adsorption of intermediates. Moreover, the high-valence Mo sites also promote the Ni-3d orbitals to a closer position to E_F, thus improves the electrochemical activity of Ni sites. Both P-3p and O-2p orbitals locate at the deep position from E_F, indicating their electron-rich features, which are able to balance the surface electroactivity to suppress the overbinding effect by Ni-H and Ni-O.

The site-dependent PDOSs of Ni-3d orbitals in O-NiMoP were further analyzed, as displayed in Fig. 7e. In comparison with metallic Ni, O-NiMoP exhibits a gradual upshifting d-band center from the near-surface sites to the surface sites. In particular, it is noted that the neighboring Mo sites further uplift the d-band center of Ni sites, thus guarantee the efficient electron transfer for both HER and UOR. In contrast, the Ni-3d orbitals of O-NiP show the barely unchanged d-band center from the middle layer to the near-surface and only a slight upshifting at surface sites (Fig. 7f), suggesting the limited active sites on O-NiP. These results indicate that the introduction of Mo atoms has significant contributions to improve the activity of O-NiMoP. Meanwhile, the P-3p orbitals of O-NiMoP also deliver an upshifting trend from the middle layer to the surface, where the coordination number of the P site affects its electronic structures (Fig. 7g). In comparison with OER, UOR involves more electron transfer with lower standard potential [12, 24]. To guarantee the efficient electrocatalysis of the complicated UOR, the rapid electron transfer is essential for the intermediate transformation process. Notably, the PDOS of the key intermediates for UOR indicates a highly linear correlation under the catalysis of O-NiMoP (Fig. 7h), which contributes to the efficient electron transfer between elementary

reaction steps. Overall, with such modulated electronic structures induced by alloying effect, the accelerated reaction kinetics and highly efficient electrocatalytic activities for both HER and UOR are expected in O-NiMoP.

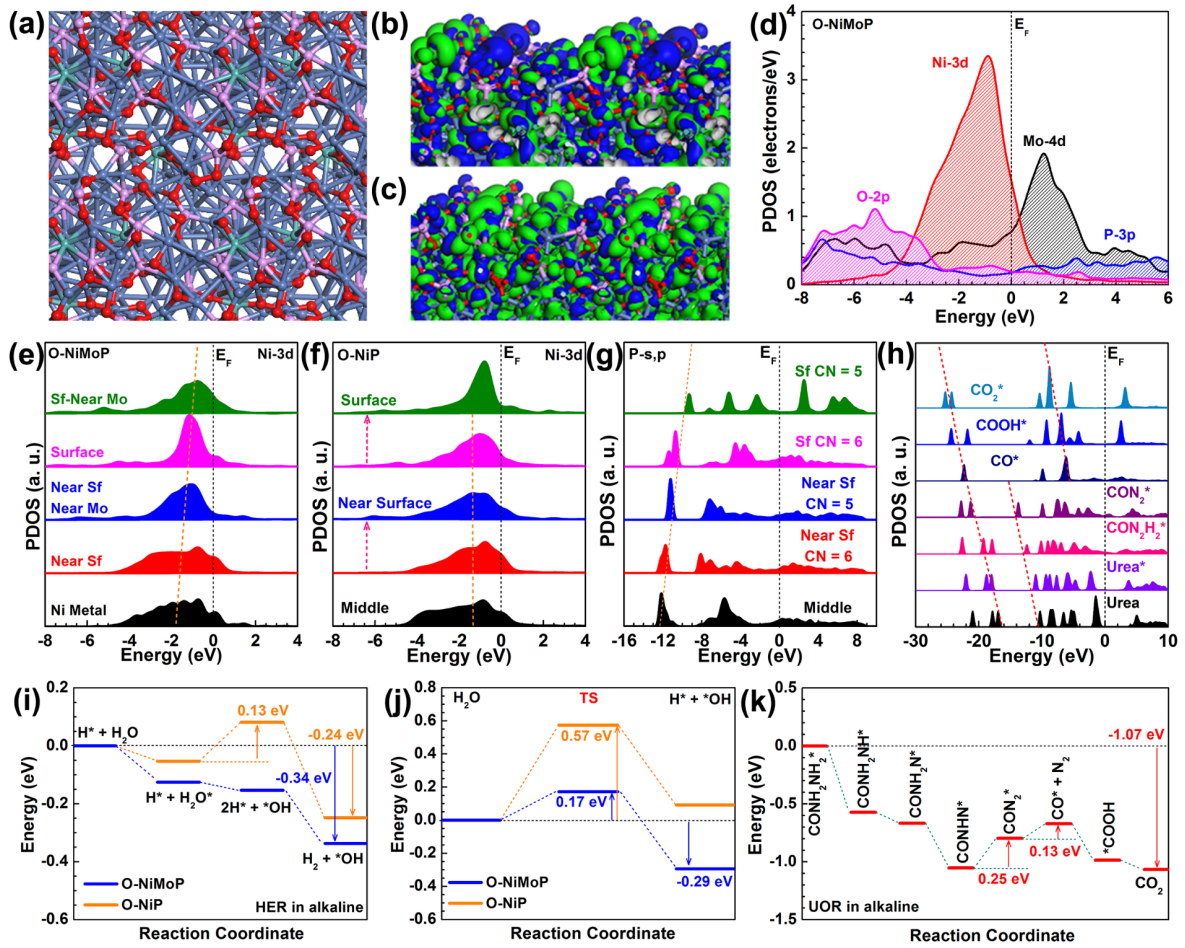

Figure 7. (a) Top view of the surface structure of O-NiMoP. Blue balls = Ni, cyan balls= Mo, pink balls = P, red balls = O. The 3D contour plot of the anti-bonding and bonding orbitals near E_F of (b) O-NiMoP and (c) O-NiP. Blue isosurface = bonding orbitals, green isosurface = anti-bonding orbitals. (d) PDOSs of Ni, Mo, P, and O in O-NiMoP. The site-dependent PDOSs of Ni-3d in (e) O-NiMoP and (f) O-NiP. (g) The site-dependent PDOSs of P-3p in O-NiMoP. (h) The PDOSs of key intermediates of UOR under the catalysis of O-NiMoP. (i) The energetic pathway comparison of HER on O-NiMoP and O-NiP. (j) The comparison of water dissociation capability on O-NiMoP and O-NiP. (k) The energy pathways of UOR on the O-NiMoP.

The energies of both HER and UOR reaction pathways were further calculated under the alkaline environment. For the HER, a strong spontaneous thermodynamics trend under the catalysis of O-NiMoP can be observed (Fig. 7i). Due to the highly active Ni sites, the generation of H_2 on O-NiMoP is exothermic with 0.34 eV heat release. In contrast, the HER on O-NiP displays an evident barrier of 0.13 eV at the step of [H^*+ H_2O^*] to [$2H^*$+*OH], which lowers the overall reaction efficiency. Therefore, the overall HER reaction trend on O-NiMoP is preferred than that on O-NiP, supporting its stronger electrochemical activity for HER. Previous studies have demonstrated that water dissociation through the Volmer step (Equation S11) is vital for the subsequent recombination of adsorbed H^* to generate H_2 in alkaline media. Thus, the water dissociation capability under the catalysis of O-NiP and O-NiMoP was further analyzed. As shown in Fig. 7j, the water dissociation energy barrier on O-NiMoP (0.17 eV) drops by two-thirds than that on O-NiP (0.57 eV), suggesting that the sluggish Volmer step on O-NiP is greatly accelerated after the introduction of Mo atoms. As for UOR, the initial dehydrogenation from the adsorbed urea molecules [$CO(NH_2)_2^*$] to [$CONH_2N^*$] displays a spontaneous reaction with an energy decrease of 0.57 eV (Fig. 7j). On the other hand, the further dehydrogenation of [$CONHN^*$] and the subsequent conversion to [CON_2^*] undergo the energy barriers of 0.25 eV and 0.13 eV, respectively, which implies that these two steps are slow processes in electrocatalytic UOR. However, the overall UOR process is still energetically favorable with an energy release of 1.07 eV, supporting a strong reaction trend under the catalysis of O-NiMoP.

Conclusions

In summary, the O-NiMoP/NF bifunctional electrocatalyst for UOR and HER is successfully synthesized by a facile electrodeposition process accompanied by *in-situ* template etching. Due to the unique nanotube array architecture and modulated electronic structure of

O-NiMoP, the as-prepared O-NiMoP/NF electrodes exhibit remarkable electrocatalytic activities and strong durability toward both HER and UOR. DFT calculations unravel that the neighboring Mo, P and O atoms significantly activate and improve the activity of Ni sites in O-NiMoP, thus accelerate the water dissociation of HER and balance the intermediates transformation of UOR. Benefiting from the superior HER/UOR activities of O-NiMoP/NF electrodes, the urea-assisted electrolysis hydrogen production system exhibited a significantly decreased cell voltage of 1.55 V at the current density of 50 mA cm^{-2} in 1.0 M KOH with 0.5 M urea, which is approximately 300 mV lower than that of the conventional water electrolysis. This work not only presents an efficient electrocatalyst for energy-saving hydrogen production with urea-assisted electrolysis, but also provides a facile strategy to synthesize active electrode materials in specific 3D nanotube array configuration which may benefit other energy storage and conversion applications.

Supporting Information

Supporting Information is available from the online version or from the author.

Acknowledgements

This work is supported by General Research Fund (CityU 11308120 and CityU 11307619), National Natural Science Foundation of China (Project No. 51872249; 21771156).

References

[1] Z.W. Seh, J. Kibsgaard, C.F. Dickens, I. Chorkendorff, J.K. Nørskov, T.F. Jaramillo, Combining theory and experiment in electrocatalysis: Insights into materials design, Science, 355 (2017) 146-158.
[2] J.A. Turner, Sustainable hydrogen production, Science, 305 (2004) 972-974.
[3] X. Yu, Z.-Y. Yu, X.-L. Zhang, Y.-R. Zheng, Y. Duan, Q. Gao, R. Wu, B. Sun, M.-R. Gao, G. Wang, "Superaerophobic" nickel phosphide nanoarray catalyst for efficient hydrogen evolution at ultrahigh current densities, Journal of the American Chemical Society, 141 (2019) 7537-7543.
[4] H. Jiang, J.X. Gu, X.S. Zheng, M. Liu, X.Q. Qiu, L.B. Wang, W.Z. Li, Z.F. Chen, X.B. Ji, J. Li, Defect-rich and ultrathin N doped carbon nanosheets as advanced trifunctional metal-free

electrocatalysts for the ORR, OER and HER, Energy & Environmental Science, 12 (2019) 322-333.
[5] B. Liu, Y.F. Zhao, H.Q. Peng, Z.Y. Zhang, C.K. Sit, M.F. Yuen, T.R. Zhang, C.S. Lee, W.J. Zhang, Nickel-cobalt diselenide 3D mesoporous nanosheet networks supported on Ni foam: an all-pH highly efficient integrated electrocatalyst for hydrogen evolution, Advanced Materials, 29 (2017) 1606521.
[6] L. Li, P. Wang, Q. Shao, X. Huang, Metallic nanostructures with low dimensionality for electrochemical water splitting, Chemical Society Reviews, (2020).
[7] Y. Li, X. Wei, L. Chen, J. Shi, M. He, Nickel-molybdenum nitride nanoplate electrocatalysts for concurrent electrolytic hydrogen and formate productions, Nature communications, 10 (2019) 1-12.
[8] C. Li, Y. Liu, Z. Zhuo, H. Ju, D. Li, Y. Guo, X. Wu, H. Li, T. Zhai, Local charge distribution engineered by schottky heterojunctions toward urea electrolysis, Advanced Energy Materials, 8 (2018) 1801775.
[9] Z.-Y. Yu, C.-C. Lang, M.-R. Gao, Y. Chen, Q.-Q. Fu, Y. Duan, S.-H. Yu, Ni-Mo-O nanorod-derived composite catalysts for efficient alkaline water-to-hydrogen conversion via urea electrolysis, Energy & Environmental Science, 11 (2018) 1890-1897.
[10] M. Yang, Y. Jiang, M. Qu, Y. Qin, Y. Wang, W. Shen, R. He, W. Su, M. Li, Strong Electronic Couple Engineering of Transition Metal Phosphides-Oxides Heterostructures as Multifunctional Electrocatalyst for Hydrogen Production, Applied Catalysis B: Environmental, (2020) 118803.
[11] M.P. Browne, Z. Sofer, M. Pumera, Layered and two dimensional metal oxides for electrochemical energy conversion, Energy & Environmental Science, 12 (2019) 41-58.
[12] B. Zhu, Z. Liang, R. Zou, Designing Advanced Catalysts for Energy Conversion Based on Urea Oxidation Reaction, Small, 16 (2020) 1906133.
[13] Z. Dong, F. Lin, Y. Yao, L. Jiao, Crystalline $Ni(OH)_2$/Amorphous $NiMoO_x$ Mixed-Catalyst with Pt-Like Performance for Hydrogen Production, Advanced Energy Materials, 9 (2019) 1902703.
[14] L. Fei, H. Sun, R. Ran, W. Zhou, Z. Shao, Self-Supported Nickel Phosphide Electrode for Efficient Alkaline Water-to-Hydrogen Conversion via Urea Electrolysis, Industrial & Engineering Chemistry Research, 60 (2021) 1185-1193.
[15] A. Ray, S. Sultana, L. Paramanik, K. Parida, Recent advances in phase, size, and morphology-oriented nanostructured nickel phosphide for overall water splitting, Journal of Materials Chemistry A, (2020).
[16] L. Sha, J. Yin, K. Ye, G. Wang, K. Zhu, K. Cheng, J. Yan, G. Wang, D. Cao, The construction of self-supported thorny leaf-like nickel-cobalt bimetal phosphides as efficient bifunctional electrocatalysts for urea electrolysis, Journal of Materials Chemistry A, 7 (2019) 9078-9085.
[17] F. Cheng, L. Wang, H. Wang, C. Lei, B. Yang, Z. Li, Q. Zhang, L. Lei, S. Wang, Y. Hou, Boosting alkaline hydrogen evolution and Zn-H_2O cell induced by interfacial electron transfer, Nano Energy, 71 (2020) 104621.
[18] Y.K. Li, G. Zhang, W.T. Lu, F.F. Cao, Amorphous Ni-Fe-Mo suboxides coupled with Ni network as porous nanoplate array on nickel foam: a highly efficient and durable bifunctional electrode for overall water splitting, Advanced Science, 7 (2020) 1902034.

[19] M. Baek, G.W. Kim, T. Park, K. Yong, NiMoFe and NiMoFeP as Complementary Electrocatalysts for Efficient Overall Water Splitting and Their Application in PV‐Electrolysis with STH 12.3 %, Small, 15 (2019) 1905501.
[20] H.-W. Man, C.-S. Tsang, M.M.-J. Li, J. Mo, B. Huang, L.Y.S. Lee, Y.-c. Leung, K.-Y. Wong, S.C.E. Tsang, Transition metal-doped nickel phosphide nanoparticles as electro-and photocatalysts for hydrogen generation reactions, Applied Catalysis B: Environmental, 242 (2019) 186-193.
[21] B. You, Y. Zhang, Y. Jiao, K. Davey, S.Z. Qiao, Negative Charging of Transition-Metal Phosphides via Strong Electronic Coupling for Destabilization of Alkaline Water, Angewandte Chemie International Edition, 58 (2019) 11796-11800.
[22] L. Yu, I.K. Mishra, Y. Xie, H. Zhou, J. Sun, J. Zhou, Y. Ni, D. Luo, F. Yu, Y. Yu, Ternary $Ni_{2(1-x)}Mo_{2x}P$ nanowire arrays toward efficient and stable hydrogen evolution electrocatalysis under large-current-density, Nano Energy, 53 (2018) 492-500.
[23] J. Wu, D. Wang, S. Wan, H. Liu, C. Wang, X. Wang, An Efficient Cobalt Phosphide Electrocatalyst Derived from Cobalt Phosphonate Complex for All-pH Hydrogen Evolution Reaction and Overall Water Splitting in Alkaline Solution, Small, 16 (2020) 1900550.
[24] L. Zhang, L. Wang, H. Lin, Y. Liu, J. Ye, Y. Wen, A. Chen, L. Wang, F. Ni, Z. Zhou, A Lattice-Oxygen-Involved Reaction Pathway to Boost Urea Oxidation, Angewandte Chemie International Edition, 58 (2019) 16820-16825.
[25] S. Chen, J. Duan, A. Vasileff, S.Z. Qiao, Size fractionation of two-dimensional sub-nanometer thin manganese dioxide crystals towards superior urea electrocatalytic conversion, Angewandte Chemie International Edition, 55 (2016) 3804-3808.
[26] Z. Liu, X. Yu, H. Xue, L. Feng, A nitrogen-doped CoP nanoarray over 3D porous Co foam as an efficient bifunctional electrocatalyst for overall water splitting, Journal of Materials Chemistry A, 7 (2019) 13242-13248.
[27] Y. Li, X. Tan, H. Tan, H. Ren, S. Chen, W. Yang, S.C. Smith, C. Zhao, Phosphine vapor-assisted construction of heterostructured $Ni_2P/NiTe_2$ catalysts for efficient hydrogen evolution, Energy & Environmental Science, (2020).
[28] H. Sun, Z. Yan, F. Liu, W. Xu, F. Cheng, J. Chen, Self-supported transition-metal-based electrocatalysts for hydrogen and oxygen evolution, Advanced Materials, 32 (2020) 1806326.